Supporting Information

Tunable Particle-agglomeration and Magnetic Coupling in Bi-magnetic Nanocomposites

Pierfrancesco Maltoni,[*a] *Miran Baričić,* †[b] *Gianni Barucca,*[c,d] *Maria Chiara Spadaro,*[c] *Jordi Arbiol,*[e,f] *Nader Yaacou,*[b,g] *Davide Peddis,* *[b,d] *and Roland Mathieu*[*a]

1. SYNTHESIS DETAILS OF INDIVIDUAL PHASES

1.1. $Co_xZn_yFe_{3-(x+y)}O_4$ nanoparticles: thermal decomposition

The seed nanoparticles (NPs) of seeds $Co_xZn_yFe_{3-(x+y)}O_4$ were synthesized by standard airless thermal decomposition technique, as illustrated by Sun *et al.*[1]: the chemicals are listed in **Table S1**: iron(III) acetylacetonate, Fe(acac)$_3$ (99%) , Co(acac)$_2$(99%), Zn(acac)$_2$(95%), 1,2-hexadecanediol (90%), oleic acid (90%) and oleylamine (98%) were put with the desired ratio in a 100 mL round bottom two-necked flask, and dissolved in Benzyl ether (solvent). All starting materials were purchased from Sigma-Aldrich and used without further purification. The flask was connected to a Schlenk line through a 300 mm Allihn condenser and sealed at the lateral neck with a rubber septum. The system was heated in an Ar inert atmosphere, and its temperature provided by means heating mantle in a controlled way (thermocouple); the chosen thermal program is shown in **Figure S1.** Initially, the dispersion was degassed under vacuum at 110 °C for 60 min, and then it was heated up to the desired decomposition temperature (270°C) setting heating rate (5°C/min), nucleation step, and digestion time, while exposing it to inert Ar flow. Finally, the heating mantle was removed and the system was allowed to cool down to room temperature(r.t.).

Table S1. all the chemicals employed in the synthesis and their quantities are reported. The stoichiometric ratio of the organometallic precursors was adjusted according to the final desired composition.

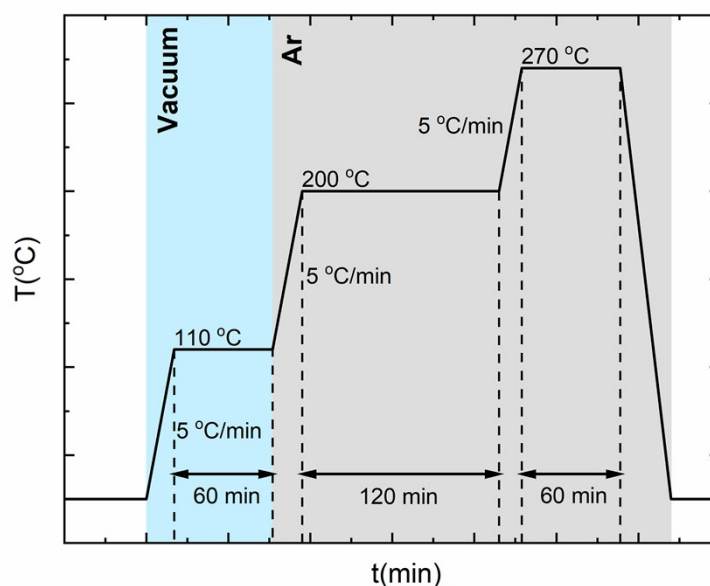| Chemical	Quantity	
Fe(acac)$_3$	2 mmol	
Co(acac)$_2$	1.29 mmol	(CFO)
	0.5 mmol	(CZFO)
	0 mmol	CFO
Zn(acac)$_2$	0.5 mmol	(CZFO)
1,2-Hexadecanediol (HDD)	10 mmol	
Oleic Acid (OA)	6 mmol	
Oleylamine	6 mmol	
Benzyl ether (DBE)	20 mL	

Figure S1. Scheme of the heating protocol during the thermal decomposition synthesis.

Once the synthesis was complete, the heating mantle was removed, waiting for the system to cool at r.t.. The NPs were washed three times with abundant ethanol and centrifugation at 4000 rpm and eventually dispersed in 8 mL of toluene. To precipitate the powders, ethanol was added into the solution, then the supernatant was discarded, and finally they were dried in a static oven at 80° C in air.

The elemental composition was confirmed by Inductively Coupled Plasma Atomic Emission Spectroscopy (ICP-AES), obtaining the results reported in **Table S2**. For each element, 1 wt% of error was estimated.

Table S2. ICP results for each element (in ppm) of CFO and CZFO, and the corresponding calculated stoichiometry.

Sample	Co (ppm)	Zn (ppm)	Fe (ppm)	Stoichiometry
CFO	$2.24 \cdot 10^5(2)$	-	$3.76 \cdot 10^5(4)$	$Co_{1.04}Fe_{1.96}O_4$
CZFO	$9.08 \cdot 10^4(9)$	$8.80 \cdot 10^4(9)$	$3.98 \cdot 10^5(4)$	$Co_{0.46}Zn_{0.40}Fe_{2.14}O_4$

Stoichiometries were calculated imposing that the summed coefficients of Zn, Co and Fe must be equal to 3. For CFO, the stoichiometry is within the experimental error for stoichiometric ferrites. According to previous studies, the small excess of iron found in the non-stoichiometric CZFO is accounted for possible $Fe^{2/3+}$ [2–4].

The elemental doping for CZFO was chosen according to our studies, confirming the maximum saturation magnetization attainable in such conditions[5].
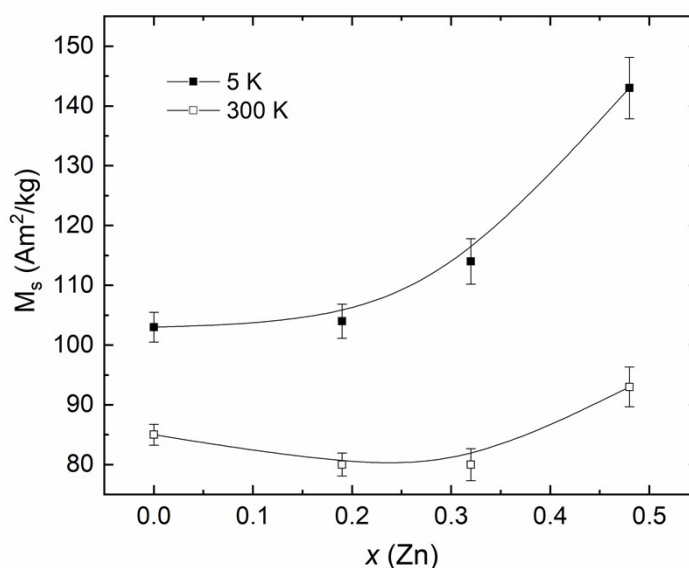
Figure S2. *Evolution of M_S at 300K and 5K for a set of CZFO NPs with similar particle size[5].*

1.2. SrFe$_{12}$O$_{19}$ nanocrystallites: sol-gel citrate self-combustion

SrFe$_{12}$O$_{19}$ (SFO) was synthesized by means of the citrate -gel self-combustion method [6], starting from metallic nitrates, whose concentrations in deionized water are listed in **Table S3**. Fe(NO$_3$)$_3$·9H$_2$O and Sr(NO$_3$)$_2$ are dissolved in deionized water with Fe^{3+}/Sr^{2+} ratio 10:1 (the Sr excess was needed to obtain pure SFO phase at lower annealing temperatures)[7]. CA 1 M solution was added so that $mol(CA) = mol(Sr^{2+}) + mol(Fe^{3+})$.

Table S3. all the chemicals involved in the pure SFO syntheses. The concentrations are calculated with respect to the total solvent amount before the ammonia solution addition.

Chemical	Concentration (mol/L)
Fe(NO$_3$)$_3$ · 9H$_2$O	$2 \cdot 10^{-1}$
Sr(NO$_3$)$_2$	$2 \cdot 10^{-2}$
CA (added as 1 M aq. solution)	$2.2 \cdot 10^{-1}$
NH$_{3(aq)}$ (28%)	-

The chemicals were mixed in a Teflon beaker at room T for 30 min with a mechanical stirrer equipped with a Teflon dash. Then the pH of the solution was adjusted to the desired value by adding concentrated NH$_4$OH$_{(aq)}$ solution dropwise, while monitoring the changing pH with a pH-meter. Three samples were synthesized at different final pH values: 4, 7 and 10 respectively. Subsequently, the beaker was immersed into a 120° C silicon oil bath until the solutions became a dry gel (~ 4 hours). Once the treatment was complete, the gel was ground in a mortar and burnt in a preheated oven at 200° C. This temperature was chosen according to the thermal gravimetry analysis (TGA) results for citric acid and for SFO gel (**Figure S3**).
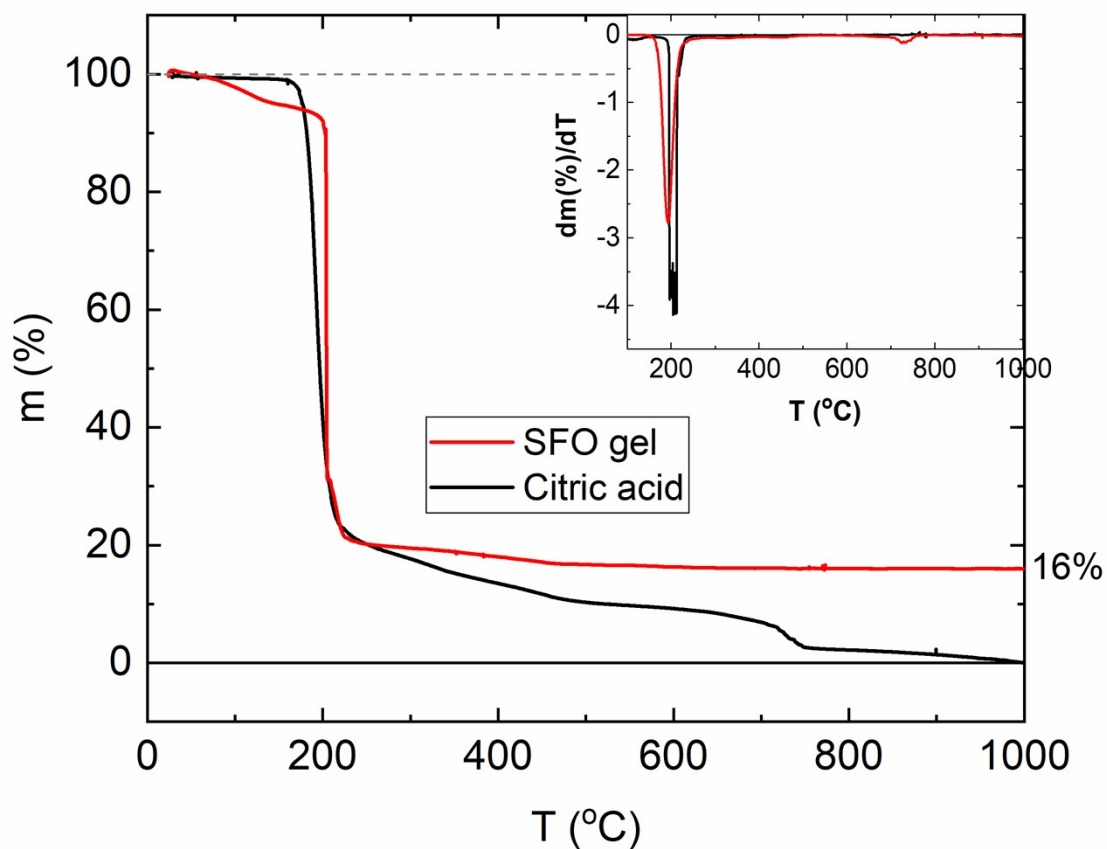
Figure S3. TG curves for an SFO *gel* and citric acid.

The resulting powders were then ground in an agar mortar: we will refer to it as SFO *as burnt*. As burnt SFOs where subsequently annealed in air: ~ 100 mg of powders were pressed with a hydraulic press, applying a ~ $6.3 \cdot 10^2$ MPa, thus obtaining cylindrical pellets and annealed at 850° C for 4 hours, with a 5° C/min heating rate. Magnetic measurements were performed on a single fragment of the pellet taken from each sample of parallelepiped-like shape, with the magnetic field applies out-of-plane.

2. STEM-HAADF AND STEM_EELS OF CZFO
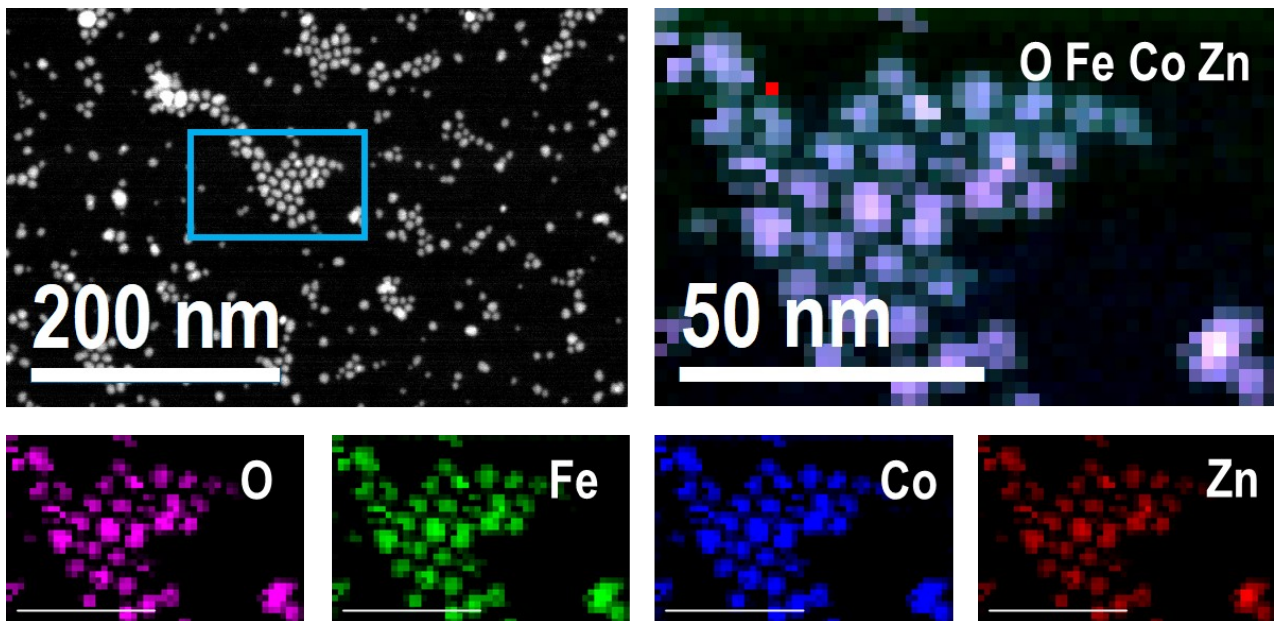
Figure S4. *STEM-HAADF and STEM-EELS compositional map of the CZFO NPs showing the right composition of the seeds and the uniform distribution of Zn. The STEM-EELS maps have been acquired considering the O K-edge at 532 eV (pink), Fe L-edge at 708 eV (green), Co L-edge at 779 eV (blue) and Zn L-edge at 1020 eV (red). Scale-bar in the single elements images is 50 nm.*

For determining the average size of the CZFO seeds, HAADF images of the nanoparticles were analyzed by the software ImageJ. A representative size was attributed to each measured nanoparticle taking as value the diameter of an equivalent circle having the same particle area. The average diameter value, which was taken as representative size, is obtained as an arithmetic average on more than 200 particles. The associated uncertainty is estimated by considering the width of the corresponding Gaussian distribution function (standard deviation).

3. XRPD AND RIETVELD REFINEMENT ANALYSIS OF INDIVIDUAL PHASES

3.1. CFO and CZFO nanoparticles

NPs apparent sizes were estimated by Scherrer equation: the FWHMs were deduced by refining the X-ray powder diffraction (XRPD) patterns (**Figure S5.**; refinement quality factors are shown in **Table S4.**), using a Thompson–Cox–Hastings pseudo-Voigt function.
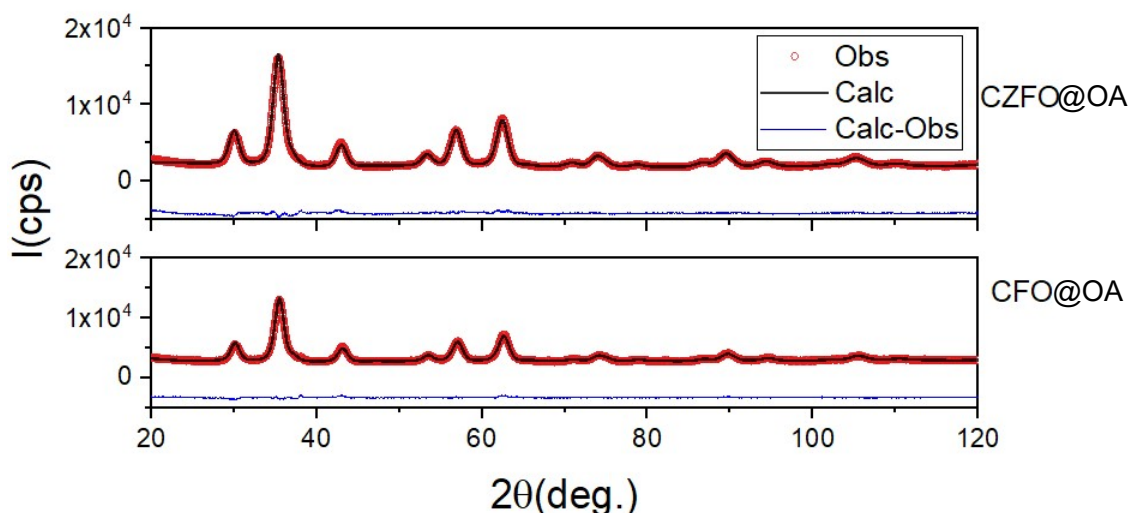
Figure S5. Rietveld refinement for the oleic acid-coated CFO@OA and CZFO@OA seeds.

Table S4. Refinement quality factors.

Sample	R_{Bragg} (%)	R_P (%)	R_{WP} (%)
CZFO	3.9	9.6	9.6
CFO	3.7	11.5	9.6

All the samples have the same average size, and after the ligand exchange, no new impurities or anomalies were detected; the small difference in average diameter between the samples before and
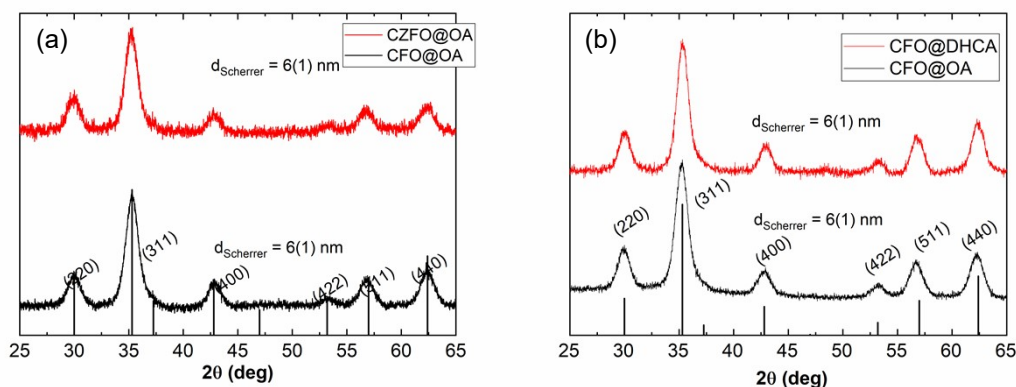
after the ligand exchange is within the experimental error.

Figure S6. (a) XRPD patterns for CFO@OA and CZFO@OA; (b) pattern for the corresponding CFO before and after the ligand exchange (CFO@DHCA).

For non-stoichiometric CFO, the lattice parameter *a* is close to 8.40 Å, not excluding to have both Co-doped maghemite NPs or also cobalt-doped magnetite phase (Fe^{2+}/Fe^{3+} oxide) where oxidation of Fe^{2+} ions did not take place[8].

3.2. SFO@pH4-7-10

XRPD patterns were measured on both as burnt and SFO samples (synthesized at different pHs) (**Figure S7**). By indexing, as burnt samples are mostly composed of maghemite, and Sr carbonates. No significant differences could be observed between the three at this stage of the preparation. However, after the annealing at 850 °C for 4 h in air, the hexagonal phase appears. All the samples clearly show the characteristic peaks of the M-type hexagonal SFO; interestingly, the sample at pH=4 shows a secondary impurity attributed to hematite. For this case, the pH is too low to have the fully deprotonated citric acid chelating agent, thus reducing its capability to chelate Sr^{2+} and Fe^{3+} nitrates and preventing the uniform distribution of precursors in the forming gel.

Figure S7. XRPD patterns of (a) *as burnt* and (b) final annealed SFO samples synthesized in different pH conditions. In (c) and (d) corresponding zoom on the region of interest.
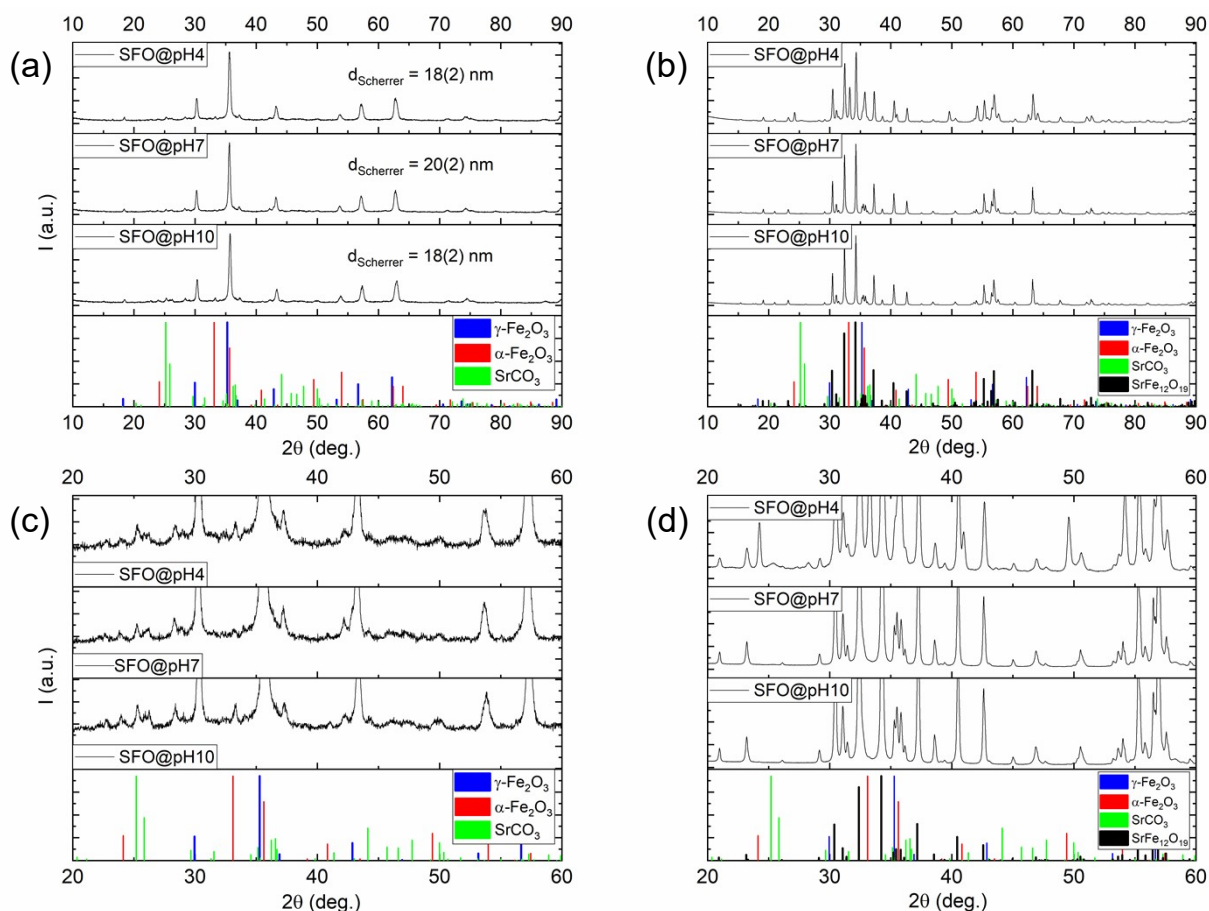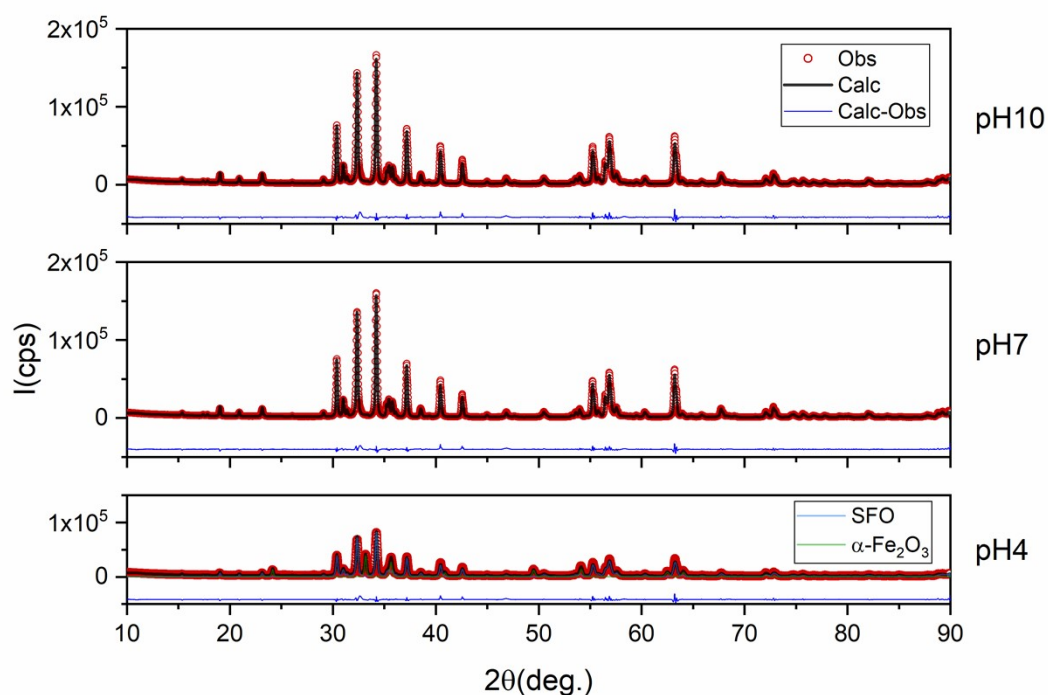
Figure S8. Rietveld refinement for SFOs.

Table S5. Refinement quality factors.

pH	R_{Bragg} (%)	R_P (%)	R_{WP} (%)
SFO@pH10	3.1	7.6	10.3
SFO@pH7	3.0	4.8	7
SFO@pH4	2.8	7.6	9.3

Results from table below seem consistent (in terms of absolute values) with the literature [9,10]. The R ratio (=d_{ab}/d_c) at pH 10 is an indication of more isotropic crystallites compared to pH=7; moreover, at pH=7 the R is higher, indicating more plate like crystallites.

Table S6. Unit cell parameters, crystallites' sizes, platelet ratio (R) and hematite wt% extracted from Rietveld analysis of XRPD patterns.

sample	pH	a=b (å)	c(å)	d_{ab}; d_c	R	α-Fe_2O_3 wt %
SFO@pH10	10	5.87879(2)	23.05107(5)	136(9); 114(5)	1.19	-
SFO@pH7	7	5.87976(1)	23.05174(4)	142(18); 104(5)	1.36	-
SFO@pH4	4	5.87794(3)	23.05541(5)	72(5); 63(2)	1.14	22(1)

4. MAGNETIC PROPERTIES OF INDIVIDUAL PHASES

4.1. Temperature-dependent magnetization of CFO@OA and CZFO@OA

ZFC/FC curves were measured in *sweep* mode at 25 Oe from 5 to 300 K. Magnetization values for each curve were divided by the lowest temperature FC value. From the ZFC/FC data elaboration, the maximum temperature, the irreversible temperature, and the average blocking temperature (T_{max}, T_{irr} and T_b respectively) can be estimated. T_{max} is obtained by calculating $d(M_{ZFC})/dT$ and finding the intercept with the temperature axis, while T_{irr} is estimated by subtracting ZFC curve from FC curve and assigning it to the temperature at which the difference drops to 3% of its maximum value. To find T_b, the procedure indicated in Concas *et al.* work[11] is followed. Briefly, the FC-ZFC curves of a batch of non-interacting particles can provide information on the sample's anisotropy energy distribution $f(T)$, as shown in the following relation [12]:

$$f(T) \propto - \frac{d(M_{FC} - M_{ZFC})}{dT}$$ (Eq.1)

At a given temperature T', the NPs can be divided into two subpopulations: the blocked particles and the superparamagnetic (SPM) ones. By integration of the areas under the $f(T)$ curve, the relative ratio of the two subpopulations, say R, can be obtained:

$$f(T) \propto R(T') = \frac{P_{SPM}(T')}{P_b(T')} = \frac{\int_{T'}^{T_{final}} f(T)dT}{\int_{T_0}^{T'} f(T)dT}$$ (Eq.2)

Where T_0 and T_{final} are the extremes of the temperature range covered during the measurement, and the average T_b for the system is the temperature at which $R(T_b) = 1$.

Once $d(M_{FC} - M_{ZFC})/dT$ curve is calculated, it can be integrated and normalized; the temperature at which this final curve reaches the 50% of its maximum value can be assigned to the average sample's T_b.
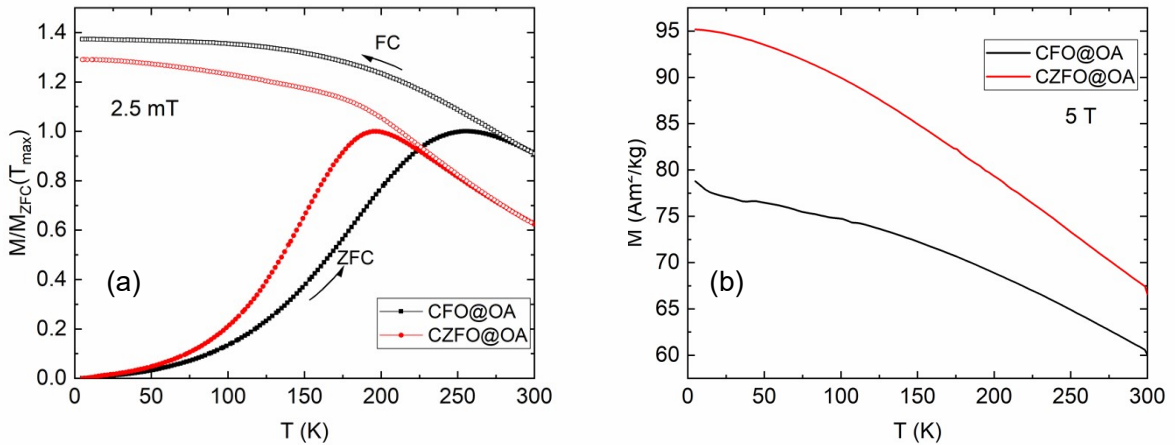
Figure S9. (a) normalized ZFC/FC curves for CFO@OA and CZFO@OA; (b) magnetization (M) vs temperature (T) recorded at 5T.

The T_b in a ferromagnetic NP can be derived from the relaxation time τ Néel-Brown equation for a non-interacting system of NPs[13]:

$$\tau = \tau_0 e^{\frac{\Delta Ea}{k_B T}} \tag{Eq.3}$$

where k_B is the Boltzmann constant, τ_0 is the characteristic relaxation time, and ΔE_a is the energy barrier between two energy minima, depending on the magnetic anisotropy constant K_a and the particle volume V ($\Delta E_a = K_a V$). From **Equation 3**, T_b can be defined as the temperature at which the relaxation time τ equals the experimental measuring time τ_m of the technique:

$$T_b = \frac{K_a V}{k_B (\ln \tau_m - \ln \tau_0)} \tag{Eq.4}$$

Since the NPs volume is the same, it is possible to attribute the blocking temperature decreasing effect of Zn^{2+} (**Table 1** in main text and **Figure S6**) to the diminishing anisotropy of the material, which is further confirmed by the seeds 5 K hysteresis loops.

4.2. M vs H curves of CFO@OA and CZFO@OA

Isothermal field-dependent magnetization curves plots (M vs μ_0H) at 5 K show the typical hysteretic behavior of a ferrimagnetic material like ours. The effect of Co^{2+} substitution with Zn^{2+} is especially visible in the coercivity reduction and on the saturation increase. These effects can be explained at a microscopic level recalling Zn^{2+} single ion properties: Zn^{2+} is diamagnetic, hence, when substituting Co^{2+}, it does not participate to the exchange interaction, thus breaking several exchange path and reducing the overall anisotropy of the material, and thus also its coercivity; the saturation instead is increased over the 0<x<0.5 interval due to the strong selectivity of Zn^{2+} for Td sites, thus reducing the Td sites contribution to the total magnetization and, due to the ferrimagnetic character of the material, increasing its overall value. A simple empirical estimation of the material's anisotropy could be given with the following equation[14]:

$$K_{eff} = \frac{\mu_0 H_K M_S}{2} \tag{Eq.5}$$

where H_K is the anisotropy field of the material. Kodama *et al.* [15] pointed out that $\mu_0 H_K \sim \mu_0 H_{sat}$, where $\mu_0 H_{sat}$ is calculated as the field where the difference between the magnetizing and the demagnetizing branches of the hysteresis loop curve is 1%[16]. To obtain K$_{eff}$ in J/m^3 a density of 5290 kg/m^3 was
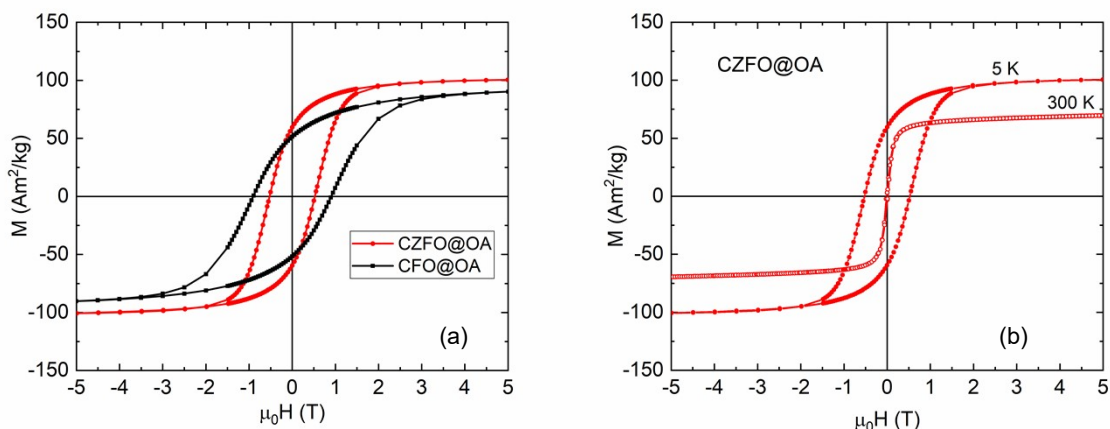
assumed for all samples. The resulting values are reported in **Table 1** in main text. Our values are comparable with the ones obtained for Co ferrite by *Muscas et al.*[17] and our studies[5].

Figure S10 (a) M vs H hysteresis loops at 5K for CFO and CZFO; (b) hysteresis for CZFO at 5 and 300K.

The magnetic data were corrected by subtracting the OA weight % obtained by TGA, and thus normalizing it for the inorganic core mass. In **Figure S11** the temperature at which we observed the mass loss (~300°C) matches the typical temperature for OA degradation in oxygen[18].
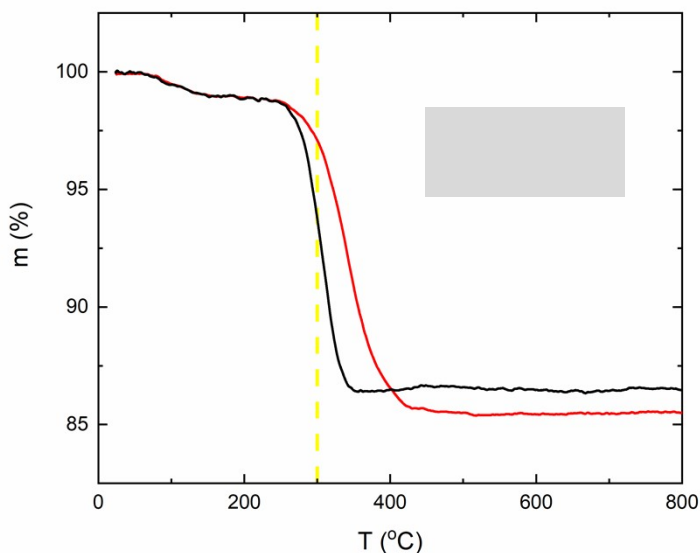
Figure S11. TGA to account for the weight % of OA coating in the normalization of magnetization.

4.3. Mössbauer spectra of CZFO@OA at 77K and 300K

The Mössbauer spectrum recorded for CZFO@OA NPs at 300K is reported in **Figure S10.**: the distribution of hyperfine fields (**Table S7.**) indicate that a large fraction of particles is in superparamagnetic state, owing the effect of thermal fluctuation, as also expected from the ZFC-FC curve (in previous section). However, at 77K there are mainly sextets with broadening and asymmetrical lines (as a result of small thermal effects that are still present since magnetometry and Mössbauer spectrometry have significantly different time scales[11]), therefore the corresponding
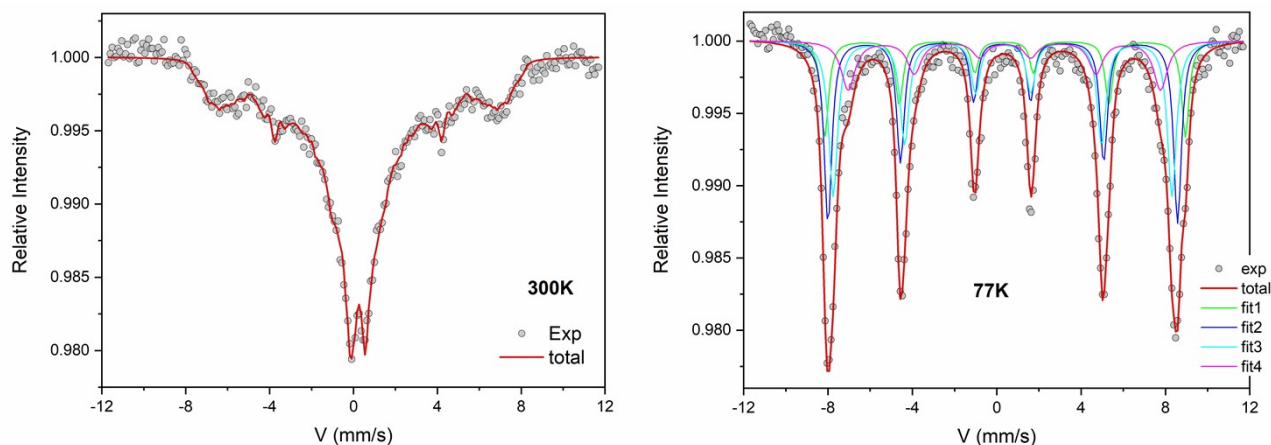
overlapping prevents to quantitively study the octahedral/tetrahedral sites distribution. The mean value of isomer shift corresponds to Fe^{3+} valence state mainly.

Figure S12. Mössbauer spectra of CZFO@OA at 300K and 77K.

Table S7. Table S12. Summary of obtained mean values of hyperfine parameters: Isomer Shift (δ), Quadrupole Shift (2ε), Hyperfine field (B_{hyp}), obtained from the fit of the spectra.

T(K)	Site	$\langle\delta\rangle$ (mms^{-1})	$\langle2\varepsilon\rangle$ (mms^{-1})	$\langle B_{hyp}\rangle$ (T)
300	Sextets Fe^{3+}(A/B)	0.38	0.02	23.1
77	Sextets Fe^{3+}(A/B)	0.48	0.004	50.1

4.4. M vs H curves of SFO@pH4-7-10

The field-dependent isothermal magnetization curves at 300K show a similar behavior for SFOs obtained at pH=7 and 10, showing that a stronger basic pH does not affect the formation of the hexagonal phase; while the one obtained using a pH=4, the magnetization drops accordingly to its hematite (antiferromagnetic phase) content.
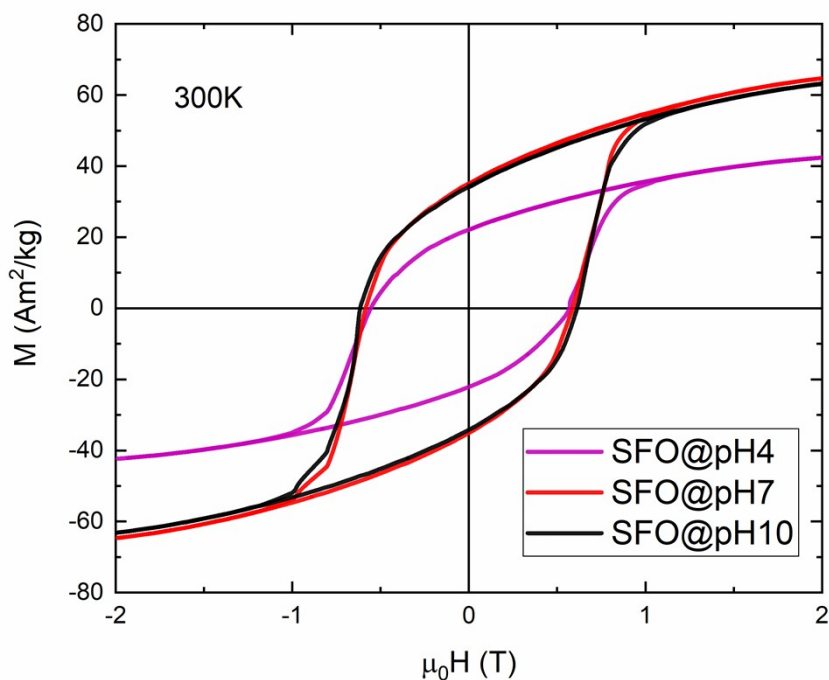
Figure S13. M vs H hysteresis loops at 300K for SFO synthesized at pH=4, 7 and 10.

5. Ligand Exchange: from hydrophobic (NPs@OA) to hydrophilic (NPs@DHCA)

A ligand-exchange process has been performed to replace the hydrophobic coating (oleic acid) with a hydrophilic layer (DHCA): ~ 150 mg of OA coated NPs were dissolved in 120 mL of THF and sonicated for 30 min in a round bottom flask; after sonication, a solution of 450 mg of DHCA in 30 mL of THF was added to the NPs dispersion. The flask was then put in a water bath kept at 60° C and stirred. After 4 h, 6 mL of 0.5 M NaOH$_{(aq)}$ solution plus 15 mL of THF were added to totally dissociate protons from DHCA molecules and extract the NPs in a water solution, where they are now soluble (and electrostatically stable thanks to the ligand); then it is left on a permanent magnet for 45 min: after this the supernatant is removed and more THF is added (repeated twice). The resulting powder-like particles from the precipitation after 30 min were washed several times by dispersing them in few mL of water and ~ 50 mL of isopropanol (iPrOH) and dried overnight in an oven in air. The mass normalized M vs H curves for the samples after the ligand-exchange process do not show any alteration (**Figure S14**).
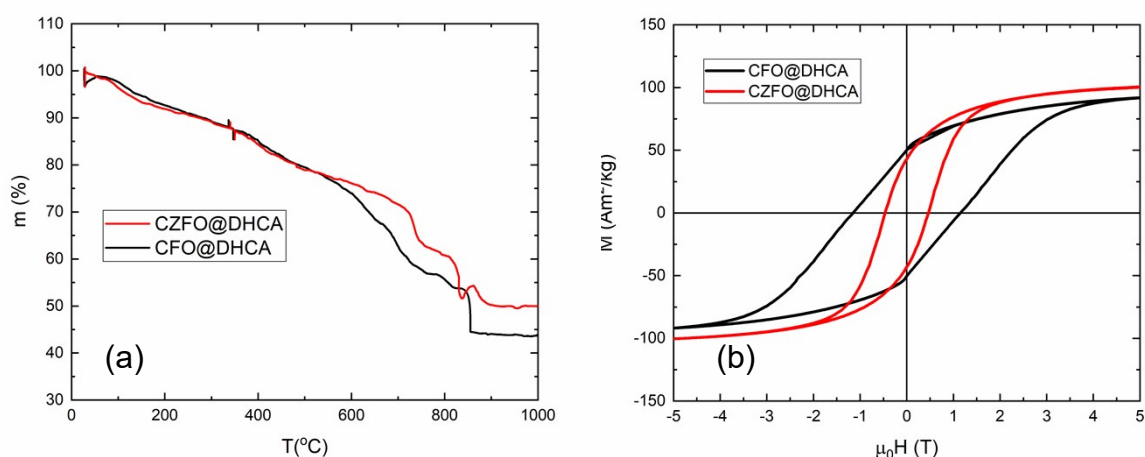

Figure S14. (a) TGA to account for DHCA content; (b) hysteresis for CFO@DHCA and CZFO@DHCA after ligand exchange.

6. DLS OF NPs@DHCA AT pH=7-10

DLS measurements were performed with a Malvern Zetasizer Nano ZSP equipped with a 10 mW He-Ne red laser (632.8 nm), operating in backscattered geometry (173°). The solutions were analyzed in plastic disposable cuvettes after filtration and sonication. The measurements, shown in **Figure 1** in the main text, are an average of five runs. The DLS works by illuminating a cuvette containing the sample with a laser beam, and detecting the scattered light with its intensity at a known angle θ. The Brownian motion of the NPs causes constructive and destructive interference phenomena which make the light intensity I(t) fluctuate over time. The DLS, by means of a software or a digital correlator, correlates the fluctuating signal over brief decay intervals τ, thus obtaining the *intensity autocorrelation function*, which for a monodisperse set of particles is:

$$G(\tau) = 1 + b \cdot e^{-Dq^2\tau} \qquad \text{(Eq.6)}$$

Where b is a constant depending on the instrument, D is the diffusion coefficient, and q is the light scattering vector, depending on the laser wavelength, the refractive index of the solvent, and the scattering angle θ. The decay of the intensity correlation over τ is usually plotted as *raw correlation function* RCF[19]:

$$RCF = G(\tau)^2. \qquad \text{(Eq.7)}$$
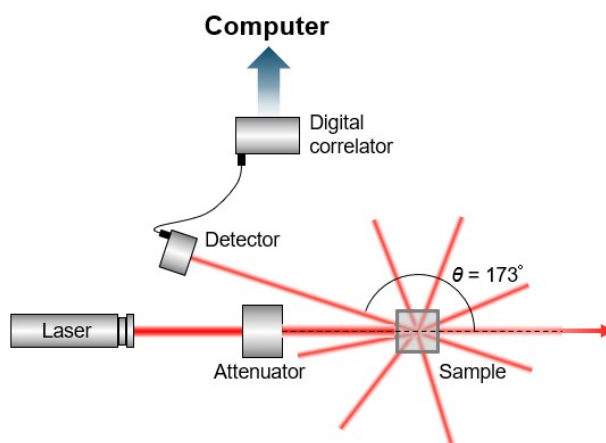
Figure S15. Schematics of DLS instrument working in backscattered geometry.

We have measured DHCA-coated particles at pH 7 and pH 10. the correlation function decay can be observed in the main paper. For a population of small nanoparticles, the corresponding signal will fluctuate faster and the *RCF* of the sample will decay over a shorter time. The opposite is true for bigger objects. A single NPs distribution will have a single *RCF* decay, while for bimodal distributions' decay consists of multiple steps[20]. In our case, the pH 7 measurement clearly shows the presence of two steps, with the second being caused by NPs agglomeration with time. This is interpreted as an increased colloidal stability of the water suspension at pH 10.

7. SYNTHESIS DETAILS OF NANOCOMPOSITES (NCs)

The synthesis was performed in the same way as the pure SFO, with the only exception of the seed NPs (previously stabilized in a NaOH aqueous dispersion) addition, that was conducted while adjusting the pH of the dispersion. The spinel ferrite seeds were introduced in the system as water dispersed nanoparticles covered in DHCA. Owing to the acidic character of DHCA, a higher pH causes a higher degree of deprotonation, and thus an increase of negative charges on the NPs' surface, thus increasing electrostatic repulsion (i.e. stability). The pK_as of DHCA are 4.5, 9.4 and 11.7[21]. Since the molecules of DHCA are likely attaching the surface from both the carboxylic and the catecholic sides without much selectivity[22], a pH of 10 allows to remove at least one proton from more than 50% of the molecules attached from the carboxylic side, increasing the colloidal stability (when an acid is in a solution where pH = pK_a, the number of protonated and deprotonated molecules is the same). Higher pH values were not reached to prevent the precipitation of Fe hydroxides [23]. The rest of the whole procedure (i.e., annealing conditions) was kept the same as for pure SFO samples.

7.1. CFO wt% FRACTION QUANTIFICATION IN NCs

The CFO/(CFO+SFO) w/w ratio was calculated by means of X-ray Fluorescence (XRF). From the experimental data, which are given in mass percentage of metallic species, the amount of cobalt ferrite is calculated on the basis of Co+Zn=1 mol, which corresponds to the CZFO moles. The SFO quantity instead can be calculated in two ways: the first by considering the Sr moles, which due to the stoichiometry of $SrFe_{12}O_{19}$ are equal to the SFO moles; the second way consists in subtracting the Fe moles constituting CFO (twice the Co+Zn sum) to the total Fe moles and using what remains to calculate the SFO amount. By using pure stoichiometric SFO sample, we determined that Sr quantity is underestimated by our instrument, with its Fe/Sr ratio being 13.4 instead of 12. The Sr experimental quantities (shown in **Table S6**) were thus multiplied for a 13.4/12 correcting factor to compensate the erroneous Sr determination.

Table S8. Experimental mass percentages (wt %) of each element and C(Z)FO.

Sample	Fe (%)	Co (%)	Zn (%)	Sr (%)	C(Z)FO (%) (1st method)	C(Z)FO (%) (2nd method)
NC@CFO@pH10	87.0	3.4	0	9.6	8.6	8.5
NC@CZFO@pH10	87.7	1.6	1.0	9.7	7.2	7.2
NC@CZFO@pH7	91.5	1.6	1.0	10.2	6.9	6.9

The two calculation pathways give very similar results, suggesting the reliability of the method. Also, with the correction, the Fe/Sr ratio (without considering the Fe contained in the spinel phase) at the synthesis end is approximately 12 for all the samples, meaning that the synthesis provides a good phase purity.

8. STRUCTURAL PROPERTIES OF NCs

8.1. XRPD and Rietveld refinement analysis

The seed weight fraction was chosen after conducting several experiments in different conditions, to reveal possible thresholds which might affect the growth of SFO phase during the annealing step. The complete transformation from SFO's precursors to the pure phase (with neglectable secondary impurities), was detected up to 10 weight %; in contrast, a 20% does not permit the total conversion. For this reason, a content <10% spinel-like phase content was chosen, while still having a reasonable amount of cobalt ferrite to be detected and characterized.
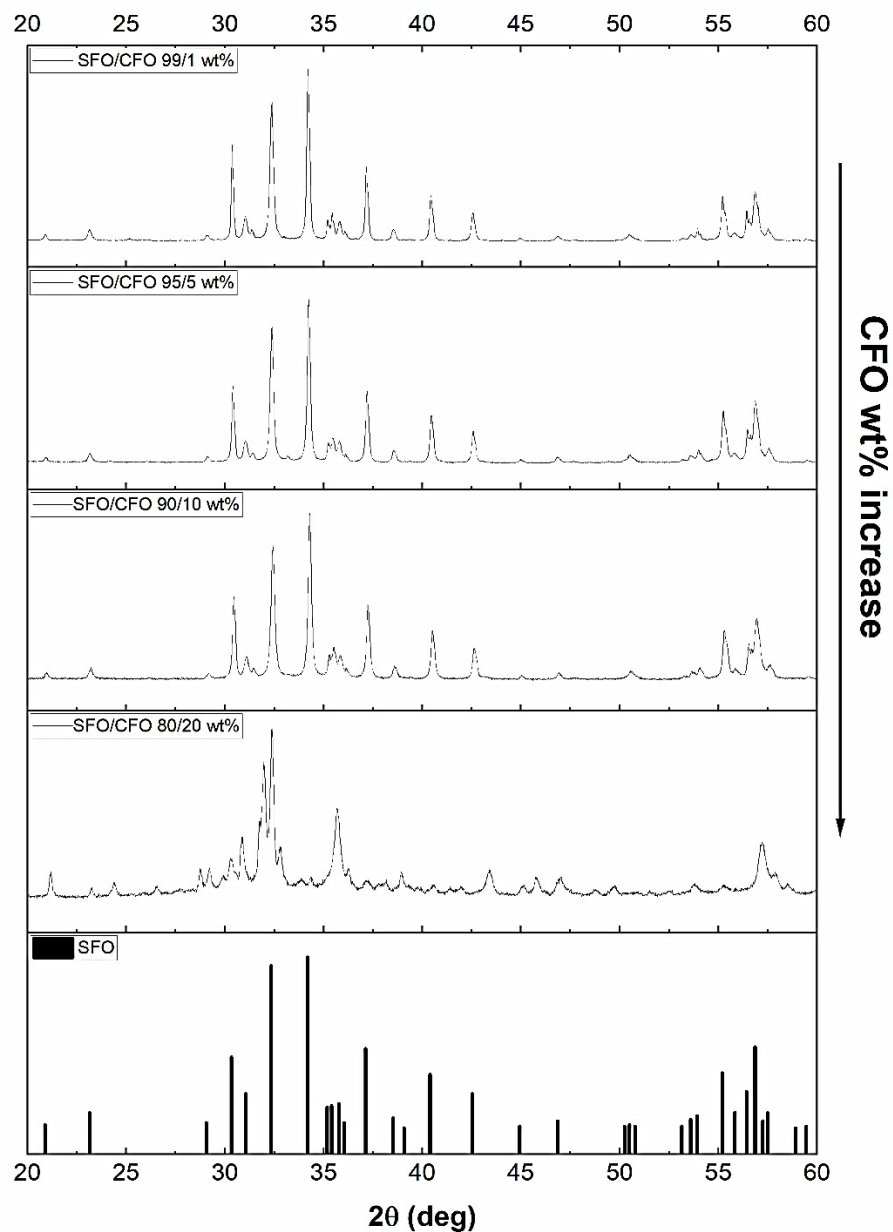
Figure S16. SFO/CFO nanocomposites at different CFO weight percentages.

SFO sizes are comparable at pH=10 for CFO and CZFO phases, while at pH=7 they are bigger, as also observed for individual SFO obtained at that pH (as expected). However, spinel seed particles undergo a drastic increase in size from 32 to 57 nm (nearly double) as the pH decreases: this effect is ascribed to the low colloidal stability at pH 7 of the ligand which covers CFO particles. At pH=10 the second pK_a is overcome and the complete deprotonation of the ligand is guaranteed, thus keeping the CFO particles more well separated.

For NC@CZFO@pH7, an effort to introduce an additional phase ($Sr_4Fe_6O_{13}$) in the Rietveld refinement was not successful, because of the wt% is too close to the resolution limit of the instrument, and the many parameters are cross correlated.

Table S9. Refinement quality factors.

Sample	R_{Bragg} (SFO/C(Z)FO) (%)	R_P (%)	R_{WP} (%)
NC@CZFO@pH10	2.3/2.1	7.2	7.9
NC@CZFO@pH7	3.3/2.8	7.6	9.4
NC@CFO@pH10	3.2/2.9	7.4	9.0

8.2. TG analysis

TG curves were recorded for the nanocomposites after the annealing procedure. For the composites at pH=10, we do not observe large deviations, which are presumably due to a structural rearrangement after the second annealing provided by the measurement itself. On the other hand, for the sample obtained at pH=7 we observed a ~10% weight loss, thus strengthening the results from XRPD analysis which indicated the presence of Sr^{2+} carbonate in that sample, and different ferrite-phases that can be rearranged upon thermal treatment.

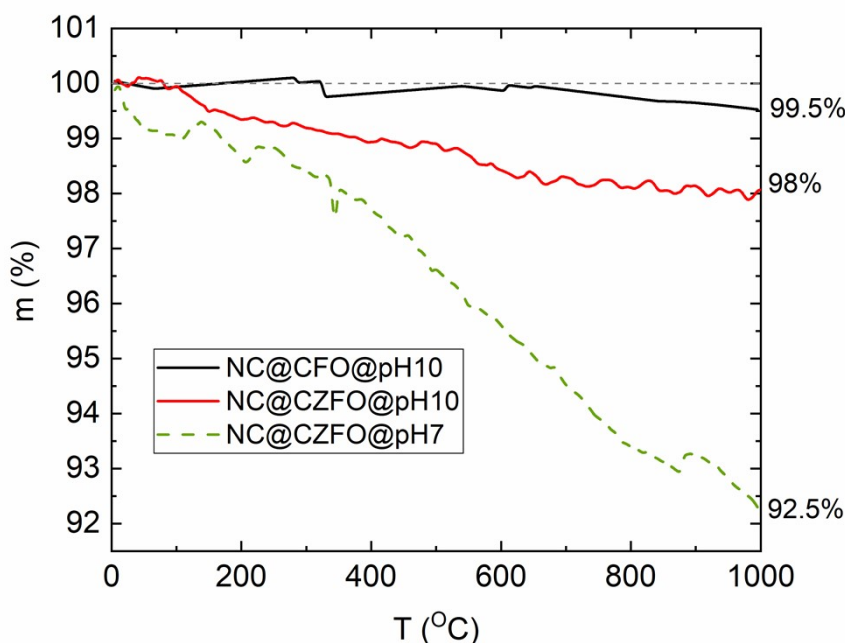**Figure S17.** TG curves of the annealed nanocomposites with the selected spinel ferrites.

8.3. Effect of annealing step on CZFO seeds in NCs

The possible segregation of oxides from the spinel CZFO in the composite, while thermally treated, was evaluated by annealing CZFO in air at 850°C for 4h (as the composites). It was found that an amount of 11 weight % of hematite is segregated, in good agreement with the estimated amount

from the Fe^{x+} excess in this seed (~13 weight %). Interestingly, the CFO seed (stoichiometric) did not show any sign of secondary impurities.
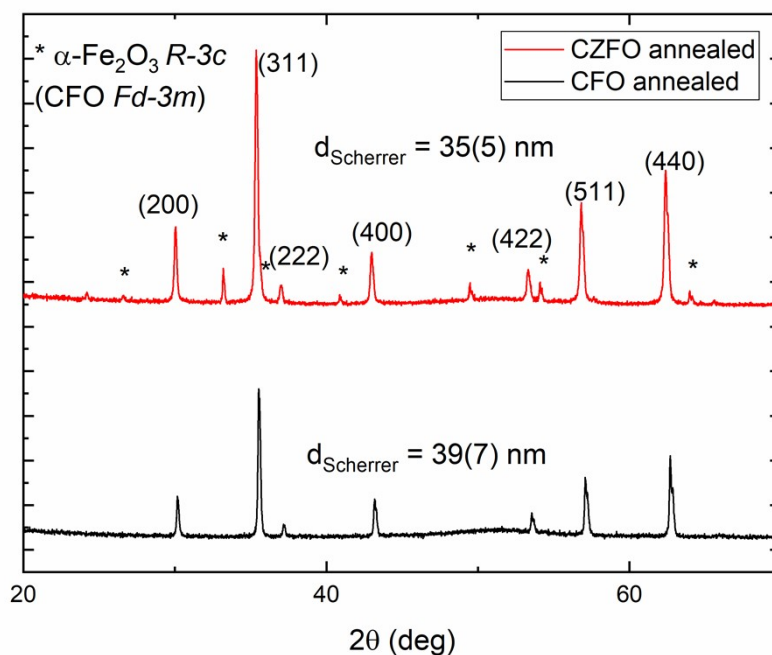

Figure S18. Annealed CFO and CZFO seeds in the same conditions as composites.
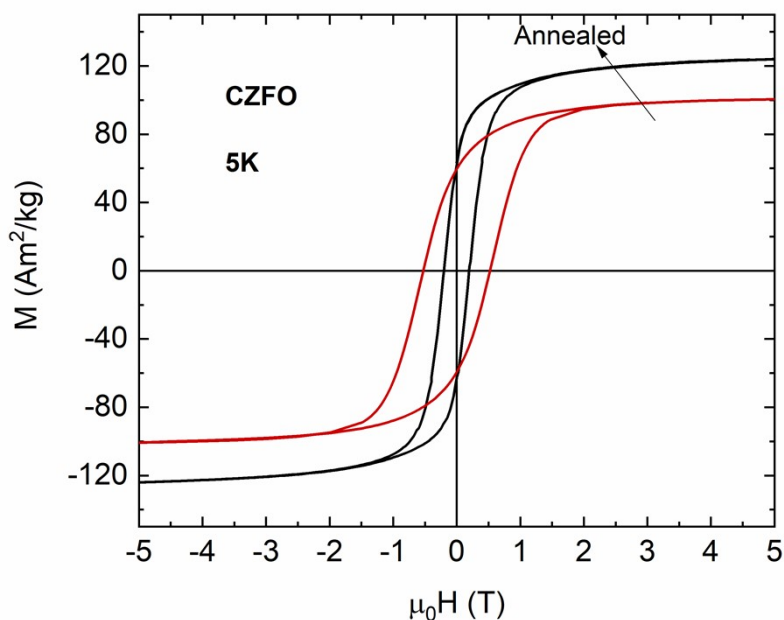

Figure S19. M vs H hysteresis loops at 5K for CZFO and annealed CZFO.

Table S10. Lattice parameters for CZFO and CFO as seeds, annealed seeds and in the NCs.

Id	$a_{in\ seed}$ (Å)	$a_{in\ NC}$(Å)
CFO@pH10	8.3954(2)	8.4020(1)
CZFO@pH10	8.4091(2)	8.4251(1)

		[annealed 8.4162(5)]			
CZFO@pH7		II			8.4225(2)

8.4. Mössbauer spectra of NC@CZFO@pH7-10 at 77K and 300K

The spectrum of NC@CZFO@pH10 recorded at 300K was fitted by 5 sextets in agreement with the 5 Fe^{3+} sites typical of SFO: 3 octahedral ($12k^{SFO}$, $4f2^{SFO}$, $2a^{SFO}$), 1 tetrahedral ($4f1^{SFO}$) and 1 bipyramidal ($2b^{SFO}$). The hyperfine field at ^{57}Fe nuclei for all positions is different and has the following order: $B_{hyp}Fe(4f2) > B_{hyp}Fe(2a) > B_{hyp}Fe (4f1) > B_{hyp}Fe (12k) > B_{hyp}Fe (2b)$ at room T°. Also, we cannot exclude a small contribution given by the overlapping particles of CZFO on the % of fit 1, 2, 3 and 4. In addition, a doublet (CZFO!) was assigned to possible isolated small CZFO particles of ferrite that may still maintain a superparamagnetic behavior (note that the probed time scales are different in Mössbauer spectrometry, compared to magnetometry, specifically the dc magnetization blocking temperature should be smaller and thus particles that seem unblocked from Mössbauer, may be magnetically blocked).

At 77K, we observed a reduction of the % of the doublet from 8 % to 3 %, strengthening the assignment of the doublet observed at 300K to superparamagnetic particles of CZFO.

Table S11. Summary of obtained values of hyperfine parameters: Isomer Shift (δ), Quadrupole Shift (2ε), Hyperfine field (B_{hyp}), and percentage (%) for each site obtained from the fit of the spectra.

T(K)	Site	$\langle\delta\rangle$ (mms^{-1})	$\langle 2\varepsilon\rangle$ (mms^{-1})	$\langle B_{hyp}\rangle$ (T)	%
300	Fit1 - $4f2^{SFO}$	0.38	0.27	51.3	15
	Fit2 - $2a^{SFO}$	0.36	0.13	50.1	6
	Fit3 - $4f1^{SFO}$	0.24	0.18	48.5	17
	Fit4 - $12k^{SFO}$	0.36	0.41	41.2	47
	Fit5 – $2b^{SFO}$	0.29	2.15	40.7	7
	Fit 6 – CZFO!	0.37	0.80	0	8
77	Fit1 - $4f2^{SFO}$	0.48	0.21	54.2	15
	Fit2 - $2a^{SFO}$	0.50	0.31	54.6	6
	Fit3 - $4f1^{SFO}$	0.37	0.15	51.9	23
	Fit4 - $12k^{SFO}$	0.48	0.42	51.0	47
	Fit5 – $2b^{SFO}$	0.31	2.23	43.3	6
	Fit 6 – CZFO!	0.43	0.78	0	3

The spectrum of NC@CZFO@pH7 recorded at 300K reveals a similar trend of the SFO components to that of NC@CZFO@pH10, mainly sextets, except for (i) the absence of the doublet previously detected for CZFO and (ii) the corresponding change of % in SFO components due to the overlapping CZFO particles (larger at pH=7 than those at pH=10, and thus more presumably thermally blocked). The reduction of the % for $12k^{SFO}$ may be attributed to the latter, and thus can be used to estimate the hexaferrite wt% (around 88%) ($12k^{SFO}$ represents about 50 -52 % in pure hexaferrite[24]).

Table S12. Summary of obtained values of hyperfine parameters: Isomer Shift (δ), Quadrupole Shift (2ε), Hyperfine field (B_{hyp}), and percentage (%) for each site obtained from the fit of the spectra.

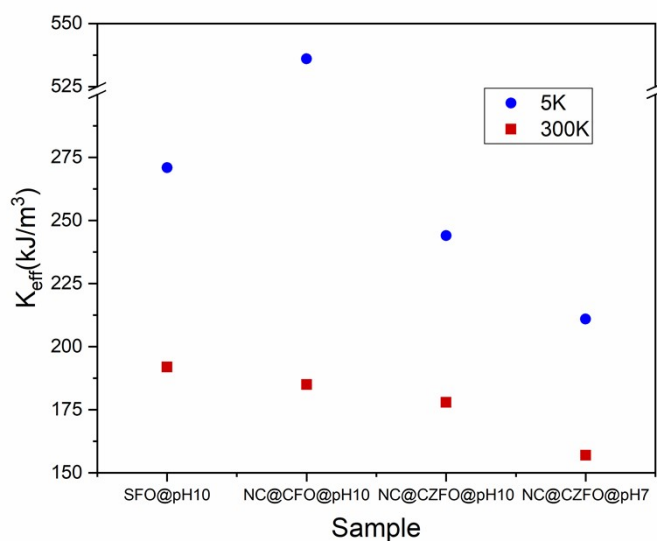| T(K)	Site	$\langle \delta \rangle$ (mms^{-1})	$\langle 2\varepsilon \rangle$ (mms^{-1})	$\langle B_{hyp} \rangle$ (T)	%
	Fit1 - 4f2^{SFO}	0.40	0.10	52.0	12
	Fit2 - 2a^{SFO}	0.37	0.12	50.6	16
300	Fit3 - 4f1^{SFO}	0.29	0.14	48.7	22
	Fit4 - 12k^{SFO}	0.36	0.40	41.1	44
	Fit5 – 2b^{SFO}	0.27	2.13	40.6	6
	Fit1 - 4f2^{SFO}	0.48	0.18	54.2	16
	Fit2 - 2a^{SFO}	0.55	0.60	53.6	7
77	Fit3 - 4f1^{SFO}	0.37	0.06	52.0	28
	Fit4 - 12k^{SFO}	0.48	0.43	51.1	43
	Fit5 – 2b^{SFO}	0.41	2.27	43.3	6

8.5. Magnetic anisotropy

Figure S20. Effective anisotropy for the samples at 300K and 5K. See section 4.3 for the definition. Note that the y-axis range was modified to highlight the variation of anisotropy.

Note that K_{eff} here is not the actual magnetic anisotropy constant, but just a simple estimate (as shown in section 4.3., Eq.5). For example, the tabulated anisotropy constant for SFO is 350 kJ/m^3 [25], while we obtain~200 kJ/m^3.

9. COMPARISON OF MAGNETIC PROPERTIES FOR SIMILAR NCs IN THE LITERATURE
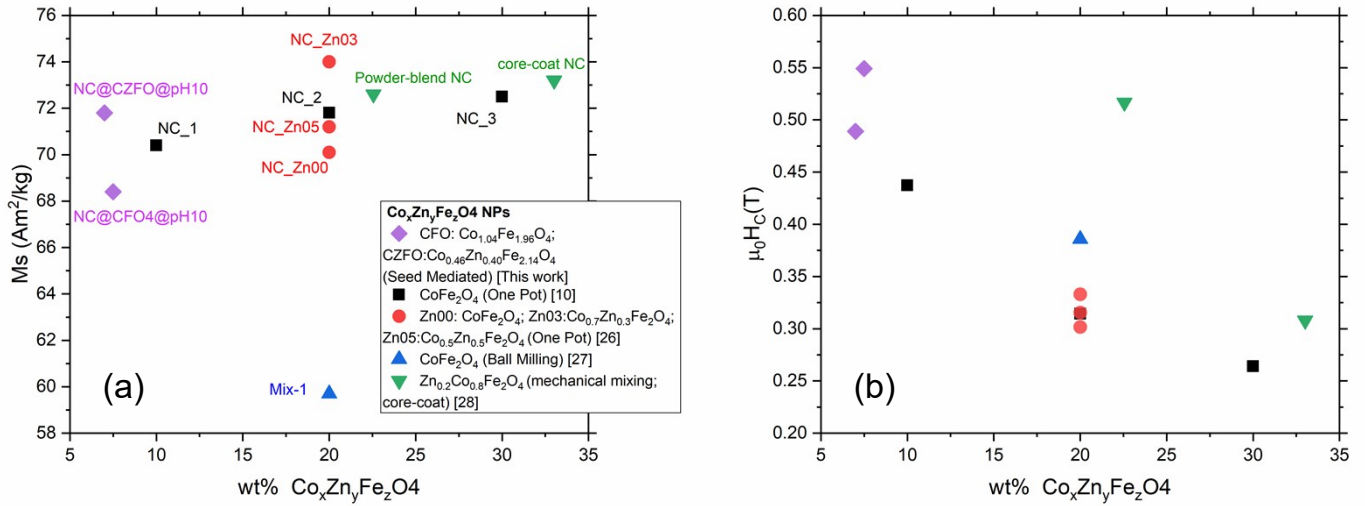

Figure S21. Literature comparison between M_S (a) and H_C (b) for composites with similar compositions.[10,26–28]

10. References

(1)   Sun, S.; Zeng, H.; Robinson, D. B.; Raoux, S.; Rice, P. M.; Wang, S. X.; Li, G. Monodisperse MFe_2O_4 (M = Fe, Co, Mn) Nanoparticles. *J. Am. Chem. Soc.* **2004**, *126* (1), 273–279. https://doi.org/10.1021/ja0380852.

(2)   Gyergyek, S.; Makovec, D.; Kodre, A.; Arčon, I.; Jagodič, M.; Drofenik, M. Influence of Synthesis Method on Structural and Magnetic Properties of Cobalt Ferrite Nanoparticles. *J. Nanoparticle Res.* **2010**, *12* (4), 1263–1273. https://doi.org/10.1007/s11051-009-9833-5.

(3)   Albino, M.; Fantechi, E.; Innocenti, C.; López-Ortega, A.; Bonanni, V.; Campo, G.; Pineider, F.; Gurioli, M.; Arosio, P.; Orlando, T.; Bertoni, G.; de Julián Fernández, C.; Lascialfari, A.; Sangregorio, C. Role of Zn^{2+} Substitution on the Magnetic, Hyperthermic, and Relaxometric Properties of Cobalt Ferrite Nanoparticles. *J. Phys. Chem. C* **2019**, *123* (10), 6148–6157. https://doi.org/10.1021/acs.jpcc.8b10998.

(4)   Muzzi, B.; Lottini, E.; Yaacoub, N.; Peddis, D.; Bertoni, G.; de Julián Fernández, C.; Sangregorio, C.; López-Ortega, A. Hardening of Cobalt Ferrite Nanoparticles by Local Crystal Strain Release: Implications for Rare Earth Free Magnets. *ACS Appl. Nano Mater.* **2022**, *5* (10), 14871–14881. https://doi.org/10.1021/acsanm.2c03161.

(5)   Baričić, M.; Maltoni, P.; Del Tedesco, A.; Barucca, G.; Canepa, F.; Mathieu, R.; Peddis, D. Correlation between Magnetic Properties and Composition/Cationic Distribution of Spinel Ferrite Nanoparticles upon Substitution by Ni^{2+} and Zn^{2+} (In Manuscript).

(6)   Danks, A. E.; Hall, S. R.; Schnepp, Z. The Evolution of "sol-Gel" Chemistry as a Technique for Materials Synthesis. *Mater. Horizons* **2016**, *3* (2), 91–112. https://doi.org/10.1039/c5mh00260e.

(7)   Maltoni, P.; Sarkar, T.; Varvaro, G.; Barucca, G.; Ivanov, S. A.; Peddis, D.; Mathieu, R. Towards Bi-Magnetic Nanocomposites as Permanent Magnets through the Optimization of the Synthesis and Magnetic Properties of $SrFe_{12}O_{19}$ Nanocrystallites. *J. Phys. D. Appl. Phys.* **2021**, *54* (12), 124004. https://doi.org/10.1088/1361-6463/abd20d.

(8)   Fantechi, E.; Campo, G.; Carta, D.; Corrias, A.; de Julián Fernández, C.; Gatteschi, D.; Innocenti, C.; Pineider, F.; Rugi, F.; Sangregorio, C. Exploring the Effect of Co Doping in Fine Maghemite Nanoparticles. *J. Phys. Chem. C* **2012**, *116* (14), 8261–8270. https://doi.org/10.1021/jp300806j.

(9)   Eikeland, A. Z.; Stingaciu, M.; Mamakhel, A. H.; Saura-Múzquiz, M.; Christensen, M. Enhancement of Magnetic Properties through Morphology Control of $SrFe_{12}O_{19}$ Nanocrystallites. *Sci. Rep.* **2018**, *8* (1), 7325. https://doi.org/10.1038/s41598-018-25662-8.

(10)   Maltoni, P.; Sarkar, T.; Barucca, G.; Varvaro, G.; Locardi, F.; Peddis, D.; Mathieu, R. Tuning the Magnetic Properties of Hard–Soft $SrFe_{12}O_{19}/CoFe_2O_4$ Nanostructures via Composition/Interphase Coupling. *J. Phys. Chem. C* **2021**, *125* (10), 5927–5936. https://doi.org/10.1021/acs.jpcc.1c00355.

(11)   Concas, G.; Congiu, F.; Muscas, G.; Peddis, D. Determination of Blocking Temperature in Magnetization and Mössbauer Time Scale: A Functional Form Approach. *J. Phys. Chem. C* **2017**, *121* (30), 16541–16548. https://doi.org/10.1021/acs.jpcc.7b01748.

(12)   Bruvera, I. J.; Mendoza Zélis, P.; Pilar Calatayud, M.; Goya, G. F.; Sánchez, F. H. Determination of the Blocking Temperature of Magnetic Nanoparticles: The Good, the Bad, and the Ugly. *J. Appl. Phys.* **2015**, *118* (18). https://doi.org/10.1063/1.4935484.

(13)   Binns, C. *Nanomagnetism: Fundamentals and Applications*; Elsevier, 2014.

(14)   Mørup, S.; Hansen, M. F.; Fradsen, C. *Magnetic Nanoparticles*; Press, A., Ed.; Amsterdam,

2011.

(15) Kodama, R. H.; Berkowitz, A. E.; McNiff, E. J.; Foner, S. Surface Spin Disorder in Ferrite Nanoparticles. *Phys. Rev. Lett.* **1996**, *77* (PART 2), 394–397. https://doi.org/10.4028/www.scientific.net/msf.235-238.643.

(16) Peddis, D.; Orrù, F.; Ardu, A.; Cannas, C.; Musinu, A.; Piccaluga, G. Interparticle Interactions and Magnetic Anisotropy in Cobalt Ferrite Nanoparticles: Influence of Molecular Coating. *Chem. Mater.* **2012**, *24* (6), 1062–1071. https://doi.org/10.1021/cm203280y.

(17) Muscas, G.; Yaacoub, N.; Concas, G.; Sayed, F.; Sayed Hassan, R.; Greneche, J. M.; Cannas, C.; Musinu, A.; Foglietti, V.; Casciardi, S.; Sangregorio, C.; Peddis, D. Evolution of the Magnetic Structure with Chemical Composition in Spinel Iron Oxide Nanoparticles. *Nanoscale* **2015**, *7* (32), 13576–13585. https://doi.org/10.1039/c5nr02723c.

(18) Mameli, V.; Musinu, A.; Ardu, A.; Ennas, G.; Peddis, D.; Niznansky, D.; Sangregorio, C.; Innocenti, C.; Thanh, N. T. K.; Cannas, C. Studying the Effect of Zn-Substitution on the Magnetic and Hyperthermic Properties of Cobalt Ferrite Nanoparticles. *Nanoscale* **2016**, *8* (19), 10124–10137. https://doi.org/10.1039/C6NR01303A.

(19) Bhattacharjee, S. DLS and Zeta Potential - What They Are and What They Are Not? *J. Control. Release* **2016**, *235*, 337–351. https://doi.org/10.1016/j.jconrel.2016.06.017.

(20) Lim, J.; Yeap, S. P.; Che, H. X.; Low, S. C. Characterization of Magnetic Nanoparticle by Dynamic Light Scattering. *Nanoscale Res. Lett.* **2013**, *8* (1), 381. https://doi.org/10.1186/1556-276X-8-381.

(21) Borges, F.; Guimarães, C.; Lima, J. L. F. C.; Pinto, I.; Reis, S. Potentiometric Studies on the Complexation of Copper(II) by Phenolic Acids as Discrete Ligand Models of Humic Substances. *Talanta* **2005**, *66* (3), 670–673. https://doi.org/10.1016/j.talanta.2004.12.012.

(22) Korpany, K. V.; Majewski, D. D.; Chiu, C. T.; Cross, S. N.; Blum, A. S. Iron Oxide Surface Chemistry: Effect of Chemical Structure on Binding in Benzoic Acid and Catechol Derivatives. *Langmuir* **2017**, *33* (12), 3000–3013. https://doi.org/10.1021/acs.langmuir.6b03491.

(23) Eikeland, A. Z.; Hölscher, J.; Christensen, M. Hydrothermal Synthesis of $SrFe_{12}O_{19}$ Nanoparticles: Effect of the Choice of Base and Base Concentration. *J. Phys. D. Appl. Phys.* **2021**, *54* (13), 134004. https://doi.org/10.1088/1361-6463/abd2ec.

(24) Maltoni, P.; Barucca, G.; Rutkowski, B.; Spadaro, M. C.; Jönsson, P. E.; Varvaro, G.; Yaacoub, N.; De Toro, J. A.; Peddis, D.; Mathieu, R. Unraveling Exchange Coupling in Ferrites Nano-Heterostructures. **2023**, *Submitted*.

(25) Coey, J. M. D. *Magnetism and Magnetic Materials*; Cambridge University Press, 2001. https://doi.org/10.1017/CBO9780511845000.

(26) Maltoni, P.; Sarkar, T.; Barucca, G.; Varvaro, G.; Peddis, D.; Mathieu, R. Exploring the Magnetic Properties and Magnetic Coupling in $SrFe_{12}O_{19}/Co_{1-x}Zn_xFe_2O_4$ Nanocomposites. *J. Magn. Magn. Mater.* **2021**, *535*, 168095. https://doi.org/10.1016/j.jmmm.2021.168095.

(27) Bilovol, V.; Sikora, M.; Martínez García, R.; Berent, K.; Gajewska, M.; Szkudlarek, A. $SrFe_{12}O_{19}/CoFe_2O_4$ Magnetic Composites: Nanoparticle Size and Effect of Annealing Temperature on Magnetic Properties. *J. Magn. Magn. Mater.* **2022**, *563*, 169987. https://doi.org/10.1016/j.jmmm.2022.169987.

(28) Shyam, P.; Mørch, M.; Eikeland, A. Z.; Ahlburg, J.; Mamakhel, A.; Saura-Múzquiz, M.; Christensen, M. Combined Characterization Approaches to Investigate Magnetostructural Effects in Exchange-Spring Ferrite Nanocomposite Magnets. *Mater. Chem. Front.* **2022**, *6* (17), 2422–2437. https://doi.org/10.1039/D2QM00091A.